THESIS

MATERIAL VALIDATION AND PART AUTHENTICATION PROCESS USING HARDNESS INDENTATIONS WITH ROBOTIC ARM IMPLEMENTATION

Submitted by

Katrina J Weinmann

Department of Mechanical Engineering

In partial fulfillment of requirements

For the Degree of Master of Science

Colorado State University

Fort Collins, Colorado

Fall 2021

Master's Committee:

Advisor: Steve Simske

Thomas Chen
Kaka Ma
Jianguo Zhao

ABSTRACT

MATERIAL VALIDATION AND PART AUTHENTICATION PROCESS USING HARDNESS INDENTATIONS WITH ROBOTIC ARM IMPLEMENTATION

In today's global economy, there are many levels of validation and authentication which must occur during manufacturing and distribution processes to ensure sufficient cyber-physical security of parts. This includes material inspection and validation during manufacturing, a method of track-and-trace for the entire supply chain, and individual forensic authentication of parts to prevent counterfeiting at any point in the manufacturing or distribution process. Traditionally, each level of validation or authentication is achieved through a separate step in the manufacturing or distribution process. In this work, a process is presented that uses hardness testing and the resulting indentations to simultaneously provide three critical functions for part validation and authentication: (i) material property validation and material property mapping achieved by administering multiple hardness tests over a given area on the part, (ii) part serialization that can be used for track-and-trace through administering hardness tests in a specific 'barcode' pattern, and (iii) the opportunity for forensic-level authentication through use of high-resolution images of the indents. Additionally, a fourth manufacturing advantage is gained in the provision of improved bonding potential for adhesive joints provided by the increase in surface area and surface roughness resulting from the addition of indents to the adherend surface. A methodology for implementing this process using a robotic arm with an end-effector-mounted portable hardness tester is presented. Implementation using a robotic arm allows a high degree of customizability of the process without changes in setup, making this

process ideal for additive manufactured parts, which are often custom or low-batch and require a higher level of material validation. As a whole, this work presents a highly-customizable, single-step process that provides multi-level quality control, validation, authentication, and cyber-physical security of parts throughout the manufacturing and distribution processes.

ACKNOWLEDGEMENTS

I would like to thank my thesis advisor, Dr. Steve Simske, for all of his guidance and support during the research presented in this thesis. I would also like to thank my committee members, Dr. Thomas Chen, Dr. Kaka Ma, and Dr. Jianguo Zhao, for the opportunity to present my thesis and their input on my work. We gratefully acknowledge the US Army Devcom Ground Vehicle Systems Center, who has approved this work with the following label:

"This material is based on research sponsored by Army Ground Vehicle Systems Center and Air Force Research Laboratory under agreement number FA8650-20-2-5700."

TABLE OF CONTENTS

LIST OF TABLES

LIST OF FIGURES

PART I: PROCESS FOR MATERIAL VALIDATION, PART SERIALIZATION, AND AUTHENTICATION USING HARDNESS INDENTATIONS

Chapter 1 – Introduction

Throughout the manufacturing and distribution processes, there are many levels of inspection and authentication which must occur in order to ensure an acceptable level of product quality and security. Such measures start at the material level, requiring validation of appropriate material properties, and extend through serialization for track-and-trace at the distribution level, and extend further to even forensic cyber-physical security of parts to prevent counterfeiting and maintain integrity throughout the supply chain. In a typical manufacturing and distribution workflow, each level of validation and/or authentication occurs separately, but this increases overall complexity because there are many different steps of validation and authentication, each measuring a different 'metric.' In Part I of this thesis, a process is presented that provides a means of simultaneous material validation, mass serialization, and the opportunity for forensic identification achieved through a single step during the manufacturing process. This is accomplished by administering hardness tests (material validation) in a grid pattern. Hardness testing leaves an indent in the surface of the material where the testing occurs. When the hardness tests are administered in a designated grid pattern, the resulting indents can then be used as a 2D barcode for serialization of the part. Furthermore, with high-resolution imagery, the patterns of indents can be analyzed, and the uniqueness between the indents can be used for forensic identification. The use of the indents for forensic validation is inherently copy-proof, because the uniqueness of each indent is a byproduct of the variability in the hardness testing process, and thus cannot be replicated. Finally, the addition of indents to the surface of the material increases the surface area and surface roughness, increasing the binding potential on the surface, and thus providing a manufacturing advantage for parts to be joined. The process of

simultaneous hardness testing and serialization via indents was tested on three different materials (acrylic, polycarbonate, and copper) and the authentication results are presented. An analysis of the indent geometry and expected increase in surface area on the marked surface is given as well.

Chapter 2 – Background

2.1 Hardness Testing

Hardness testing is a semi-destructive method of material testing used to determine the hardness of a material. It is considered to be semi-destructive because the process of hardness testing leaves an indent in the material where the test is performed. However, hardness testing is relatively non-destructive compared to other types of material testing, such as tensile testing, and thus is a very common method of testing material properties [1]. There are many different methods of hardness testing, each with its own corresponding hardness scale. Two main methodologies are behind most of the different hardness testing methods. The first, known as static indentation, is based on the idea of measuring plastic deformation under a known load to calculate material hardness. To perform this type of hardness test, an indenter tip of a specified geometry is pressed into the material at a designated load for a specified length of time. The size or depth (depending on the method) of the resulting indent is then measured to determine the amount of plastic deformation that occurred, and thus the material hardness. For this method, it is important that the indenter tip is much harder than the material being tested so that all of the deformation occurs at the surface of the material, and not at the indenter tip. Rockwell, Brinell, and Vickers hardness are some of the more common methods using this technique, and this is the most widely-used hardness testing methodology. The other common methodology for hardness testing is a dynamic, or rebound, test. To perform this test, an impact probe hits the material surface at a specific velocity, and the rebound velocity is measured and compared to the impact velocity to determine the material hardness. This method also leaves an indent where the probe impacts the material surface, but the size of the indent is not measured. The Leeb rebound test is

the main method using this technique. While these are the two main methodologies behind hardness testing, there are many variations of these methods, and various other methods of hardness testing. Other types of hardness testing include scratch hardness, abrasion and erosion testing, laboratory wear tests, and electromagnetic testing [1]. The choice of hardness testing methods depends on a variety of factors, such as the material being tested, part size, and part thickness.

Another relevant distinction in hardness testing is macrohardness versus microhardness testing. Macrohardness testing uses indenter loads of more than 1 kg, and is used mainly on large parts and thicker materials. Conversely, microhardness testing uses loads less than 1 kg, and can be used on smaller parts, and materials of thicknesses down to 0.0125mm [1]. The hardness testing discussed in this thesis will fall into the microhardness category, as the majority of additive manufactured (AM) parts are small and/or thin enough to be unable to tolerate macrohardness testing.

2.1.1 Shore Durometer Hardness

Shore durometer hardness is a method of hardness testing that was developed specifically for softer materials such as elastomers and polymers. There are 7 Shore hardness scales ranging from Shore OO (for the softest materials) to Shore D (for the hardest material that can be measured with this method). This hardness test is performed by pressing an indenter tip of known geometry into the surface of the material, and the displacement of an internal calibrated spring is measured to determine the tip displacement. Essentially, the load force on the indenter tip when pressed into the material is measured through the displacement of the spring, and this is correlated to the amount of material displaced based on the indenter tip geometry. The hardness

measurement is proportional to the tip displacement [2]. The indenter tip shape and spring constant each vary with the scale that is being used.

2.1.2 Ultrasonic Contact Impedance Hardness

Ultrasonic Contact Impedance (UCI) hardness testing uses a diamond tip indenter applied to the material surface at a known load. The hardness tester then emits ultrasonic waves and measures the difference in resonant frequency to determine the contact area, and thus the material hardness [3]. UCI hardness testing requires calibration for the material that is being tested due to a dependence of the hardness measurement on the Young's modulus of the material [4]. An advantage of UCI hardness testing is that it can be used on smaller and thinner parts than some of the more traditional hardness testing methods.

2.1.3 Hardness Testing and Material Properties

In addition to being a valuable material property to measure itself, hardness is also correlated with other material properties, such as material strength and elastic modulus. This makes measuring hardness especially advantageous because it can be used to estimate other material properties that can only be measured directly using destructive means of testing. Pavlina et al demonstrated a linear relationship between hardness and tensile strength, and hardness and yield strength in steels using diamond pyramidal hardness measurements, although at higher hardness values the hardness tended to underpredict the tensile strength [5]. Tiryakioğlu et al found a similarly linear relationship between Vickers hardness and both yield and tensile strengths in Al 7010 plates and forgings [6]. Zhang et al proposed a model for the relationship between hardness and yield strength in bulk metallic glasses [7]. Qi et al used finite element simulations to determine that Shore A and Shore D hardness are proportional to the logarithm of elastic modulus between 20A(D) and 80A(D) hardness measurements of elastomers [2].

Hardness has also been shown to be correlated with fatigue strength in various metallic alloys [8],[9].

Nanoindentation, in which small loads are applied to an indenter tip to generate nano-scale indents to measure hardness, has also been used to map out material properties in heterogenous materials. In this method of testing, the depth of the indent is measured rather than the size, eliminating the need for high-resolution imaging to determine indent size as is done in static indentation hardness testing. High-speed grid nanoindentation can be used to map out small-scale material interfaces such as welds, to perform hardness testing at very high or low temperatures, and to generate large data sets for statistical analysis of material properties. Statistical averages of nanoindentation measurements can be compared to microhardness measurements, but generally the two methods of testing can be used as complementary measurements for different aims [10].

2.1.4 Hardness Testing in Additive Manufacturing

Additive manufactured parts require more comprehensive material testing on a part-by-part basis because the material properties can vary with print settings, environmental variables, and other factors. Unlike subtractive manufacturing, where all parts made from the same batch or lot of material can be assumed to have the same material properties, each additive manufactured part must have the material properties validated individually. This necessitates a method of testing that will have a minimal impact on the structural integrity of the part. Hardness testing is a common method of validating material properties in additive manufactured parts of various materials, such as Inconel 718 [11], Ti-6Al-4V [12], and functionally graded materials [13],[14]. Hardness tests administered in grids over the surface of an additive manufactured part, similar to

the nanoindentation grids described above, can also verify homogeneity of the material properties throughout the part.

The correlation between hardness and other material properties discussed above has been demonstrated to apply to AM parts. Keist et al used hardness testing data to develop a model for the strength to hardness relationship in AM Ti-6Al-4V. They found that variations in hardness measurements across the material correlated with variations in strength measurements. They found a high variability in hardness measurements due to variances in the underlying microstructure of the material, and local orientation of the alpha phase. In their experiments, they were able to increase the accuracy of the hardness measurements by averaging 25 hardness measurements over a given area of interest, measuring the hardness to within 40 MPa with a 95% confidence level. Using this method of hardness averaging, they were able to derive a linear model relating Vickers hardness to both yield strength and tensile strength [15]. Changes in hardness measurements are also correlated to different microstructures in AM parts [16], and can be used to predict SN-curves for fatigue behavior [17].

2.2 Bonding/Joining for AM Parts

AM has provided extraordinary advances in the manufacturing space, allowing creation of parts with complex geometries, lightweight optimized parts with internal lattice structure, and more, which would be impossible to manufacture using traditional subtractive machining methods. However, one of the major drawbacks in AM is the size limitations on parts due to print bed size limitations, tolerance limits, or warping due to uneven cooling of parts. One solution to mitigate this problem is through joining of AM parts, either to other AM parts or to other subtractive machined parts. This introduces the concern of joint failure, as the location of the adhesive bond creates an additional location for potential failure of the part. To address this

concern, optimization of the strength of adhesive bonds in AM parts has been an active research area.

2.2.1 Adhesive Joint Failure

There are three modes of shear failure in adhesive lap joints, the most commonly studied form of adhesive joint: (i) adhesive failure, (ii) cohesive failure, and (iii) mixed-mode failure. Adhesive failure occurs at the bond between the adhesive and the adherend. Cohesive failure is a failure within the adhesive. Mixed-mode failure results from a combination of adhesive and cohesive failures [18]. Minimizing adhesive failure provides the greatest opportunity for increasing the bonding strength of the joint, because it involves failure in the bond between the adhesive and the adherend, and thus is not dependent on the adhesive strength. Numerous factors can affect the bonding strength of an adhesive joint, with overlap between adherends, adhesive thickness, and adherend thickness being the most influential factors [19]. Both surface area and surface roughness on the bonding surface of the joint can also affect the bonding strength of the joint. Increasing surface roughness has been shown to increase adhesive bond strength in a polypropylene copper compound [20]. Budhe et al found that shear strength of adhesive joints in aluminum and mild steel increased with abrasion of the adhesive surface up to an optimal surface roughness value, higher than which the bond strength decreased. However, all joints with surface abrasion exhibited higher bond strength than unabraded joints [21]. Baburaj et al performed laser surface modification to titanium plates and found an increase in bond strength due in part to an increase in surface area [22].

2.2.2 Adhesive Joint Optimization

Recently, research has been done investigating the possibility of optimizing the adhesive joint interface by adding features and optimizing parameters during the AM process to reduce

adhesive failure. Garcia et al 3D printed reinforcements for adhesive joints, demonstrating increases in average peak loads and shear strength values in the adhesive joints up to 8X higher than the pure adhesive joints without reinforcements. The optimized joint designs also had a much higher incidence of cohesive failure compared to adhesive failure than the pure adhesive joints [23]. Dugbenoo et al increased adhesive bond strength by using AM to print porous Nylon surfaces on the bonding surface to increase the bonding surface area. Testing showed a 550% increase in joint strength compared to conventional adhesive bonds [24]. Ubaid et al used layered/sandwich adherend tailoring to increase strength, toughness, and strain-to-break in adhesive joints [25]. Many other AM-enabled tailoring methods have also been explored to improve performance of adhesive joints [26].

2.3 Mass Serialization

Part serialization provides one level of security in the form of track-and-trace within the process of part inspection, validation, and authentication that occurs throughout the manufacturing and distribution processes to ensure cyber-physical security of a part, from manufacture to distribution to the consumer. There are three main elements required to provide security from counterfeiting in part serialization: (i) a unique ID placed on the part, (ii) a measure of copy prevention for this ID, and (iii) tamper-evidence for this ID. The unique ID, or mass serialization, serves to identify the part as the expected item. Copy prevention is achieved by creating a physical mark on the part that deteriorates in some manner when copied, so that it is evident if the mark on the part is not the original mark, and is an anti-counterfeiting measure. Tamper-evidence, also an anti-counterfeiting measure, is a feature by which it is clear if the serialization mark has been tampered with or altered in any way, indicating a breach of security in the supply chain. Usually, serialization is achieved through some kind of 1D or 2D barcode

marked on a part. Often, additional security marks are required to further achieve the goals of copy prevention and tamper-evidence necessary to provide the desired level of cyber-physical security of the part.

There are two main methods of product identification for track-and-trace purposes – barcodes and radio frequency identification (RFID). Barcodes can be subdivided into 1D and 2D barcodes, where 1D barcodes are line barcodes, and 2D barcodes encompass both stacked 2D barcodes and matrix 2D barcodes. The advantage of 1D barcodes is that they are "vertically redundant," which means that they can still be read with errors in printing because the same information is represented along each vertical line. However, 2D barcodes can convey a much higher information density than 1D barcodes, in addition to offering the possibility of using error-correcting code to retrieve information from a partially damaged code [27]. RFID tags store information, such as a serial number or SKU, that is then transmitted over radio frequencies. There are both active and passive types of RFID tags, with passive RFID tags being much more common due to their lower cost and smaller size than active tags. Passive RFID tags do not require an on-board power source, have smaller read ranges, and generally operate at lower frequencies than active RFID tags [28].

2.4 Forensic Identification

In addition to mass serialization of parts, forensic identification of individual parts is an important component of cyber-physical security and preventing counterfeiting. Forensic identification refers to identification of a specific unit of a type of part to a certainty of greater than 10^9. One method of providing a means of forensic identification is to add intentional marking(s) to the part, such as a guilloche, that gives an identification certainty sufficient for forensic level validation. This is not an ideal means of forensic identification because, since the

mark is added to the part, it is possible, though not easy, for a counterfeiter to replicate. Work has also been done to look at adding features to barcodes that can be used for forensic identification. Wang et al. looked at adding microfabricated polymeric microdots to printed barcodes for forensic identification [29]. Trenfield et al presented a combined 2D and 3D printing method for medicine tablets that incorporates the use of Ramen spectroscopy to identify covert printed materials for forensic identification in combination with printed QR codes for track-and-trace [30].

Another means of forensic validation that has been explored is using random variations in markings already on the part to achieve a forensic level of authentication. One example of this is steganography, which uses high-resolution imaging to identify edge variations in text that occur during the printing process for forensic identification [31][32]. Work has also been done to use print irregularity in barcodes to identify individual consumer products [33]. This method of forensic authentication is better because it uses random byproducts of some step of the manufacturing process as the features used for authentication, which eliminates the need for an additional step to add the forensically identifying feature, while also being nearly impossible to counterfeit because the features are created through variations in the manufacturing process, which cannot be replicated.

Chapter 3 – Materials and Methods

3.1 Hardness Testing

Material hardness testing was used to characterize the material properties of both AM and traditionally fabricated materials. Material validation is especially important for AM parts, wherein the degree of QA and QC may vary considerably between the different parties involved in the manufacture of all the different elements of an item. Material characterization includes ensuring sufficient density, validating 3D print settings, and using sensors to ensure that the desired material properties are achieved. The differences in material properties between AM and traditionally fabricated materials were tested and analyzed.

A concern with using hardness testing for material validation of additive manufactured parts is the lack of surface uniformity and relatively high surface roughness. Hardness testing is traditionally performed on flat, finished surfaces to ensure accuracy of the hardness measurement. However, it is undesirable to add a manufacturing operation to finish a surface for the sole purpose of preparing that surface for hardness testing. Here, several hardness tests were administered on the same surface to provide an average hardness value sufficiently accurate for material validation. This eliminates the need for surface finishing because any individual hardness reading variations due to surface roughness or anomalies will be averaged out by the Central Limit Theorem. Thus, this approach provides a material validation step that can be performed using the appropriate effector (human, robotic arm, etc.) for the process being performed.

Hardness tests were performed on both traditionally manufactured and AM materials. The non-AM materials tested were copper, acrylic, and polycarbonate, and the AM materials

were acrylonitrile butadiene styrene (ABS), polylactic acid (PLA), and polyethylene terephthalate glycol (PETG). Several different print configurations were tested for the AM materials. Slabs of each AM material were printed with varying porosities. The slabs were 3mm thick with the top 1.0mm and bottom 0.8mm of the slab fully dense, and the middle 1.2mm varying in porosity. The porosity was achieved with a rectilinear fill pattern, and slabs were printed fully dense, and with 10%, 20%, and 30% porosities. Additionally, cubes were printed with 2 different fill patterns at 20% porosity, and hardness tests were performed on 3 orthogonal sides to assess the anisotropic properties of the different fill patterns. The fill patterns of the cubes were rectilinear, which is expected to have anisotropic properties, and gyroscopic, which is designed to produce isotropic properties in the material.

For this experiment, two different types of portable hardness testers that are designed for use on small, thin objects were used. A Phase II PHT-980 Digital Shore D Durometer was used for the acrylic, polycarbonate, and all AM materials, and a Phase II PHT-6005 UCI (ultrasonic contact impedance) hardness tester with a 5kgf probe was used for the copper. Each of these testers is suitable for material thicknesses as low as 2 mm. These portable hardness testers were chosen for their ability to be used on small objects and the relatively small size of the test actuator, giving the ability to administer the hardness tests using a robotic arm, and decreasing the flat surface area needed for the hardness tests. Twenty hardness tests were performed on each material so the variability in the hardness measurements could be analyzed for each material.

Figure 1: Section view of AM slab geometry

3.2 Enhanced Joining

The addition of indents to the surface of a material from hardness testing increases the surface area and surface roughness of that surface, and thus improves the joining potential of that surface. The size, shape, and spatial density of the indents will determine how much increased surface area is available for joining. Using the material validation surface for bonding has the added benefit of either hiding the validation marks (if bonded to a solid material) or providing tamper protection for the serialization described in the next section (if bonded to a transparent material or forensically analyzed after failure or seizure of the object for investigatory purposes). The shape of the indent created by hardness testing is specific to the hardness tester used, and the size of the indent is affected by both the type of hardness tester and the hardness of the material being tested.

The geometry of the indenter tip of a portable hardness tester has a large impact on the increase in surface area generated by the hardness testing indents. The main factor affecting the increase in surface area per indent is the tip angle of the indenter – a smaller tip angle results in deeper indents and a larger increase in surface area. Because of this, the geometry of the indenter tip should be considered when selecting a portable hardness tester to use for this process. However, the increase in surface area is not the only way that the indents improve joining. Indents of any shape serve to rough up the surface, creating better shear behavior, and thus

enhancing the joining properties of the surface. It is more difficult to quantify the effect of surface roughness on maximum bond strength on a surface, but adherent surface roughness and adhesive bond strength have been shown to be correlated.

The indents created from three different combinations of materials and hardness testers were measured and analyzed to determine the increase in surface area for each scenario. The experiment combinations are shown in Table 1.

Table 1: Hardness tester and material combinations for indent shape analysis

Combination	Material	Hardness Tester
1	Copper	PHT-6005 UCI
2	Acrylic	PHT-980 Shore D Durometer
3	Polycarbonate	PHT-980 Shore D Durometer

3.2.1 PHT-980 Shore D Durometer

The Shore D Durometer has a conical-shaped indenter tip, with a 30° tip. The increased surface area that each indent creates can be calculated using Equation 1, where r is the radius of the indent, and θ is the tip angle of the indenter.

$$A_i = \pi r^2 \left(\sqrt{1 + cot^2 \left(\frac{\theta}{2} \right)} - 1 \right) \quad (1)$$

The percent increase in surface area can then be calculated as a function of grid spacing using Equation 2, where *d* is the nominal grid spacing, and *f* is the percentage of grid locations with an indent.

$$p_{SA} = \frac{f A_i}{d^2} X100 \quad (2)$$

3.2.2 PHT-6005 UCI

The PHT-6005 UCI hardness tester has a diamond indenter tip with an angle of 136°. The increased surface area created by an indent with this intender shape can be calculated using Equation 3, where *w* is the width of the of the indent measured perpendicular to the edges, and θ is the tip angle.

$$A_{i,t} = w^2 \left(\csc\left(\frac{\theta}{2}\right) - 1 \right) \tag{3}$$

3.2.3 Joining Configurations

There are three different configurations in which the hardness testing indents can be used for enhanced joining. The first is to administer the hardness tests on one of the two joining surfaces. This is the most likely configuration, and is ideal if only one of the two surfaces being joined required material property validation. However, of the three configurations that will be described, it is expected this configuration would provide the smallest increase in bonding potential, since it increases the total bonding surface area the least. The second configuration option is to have complementary indentations. In this case, indentations would be created on both of the joining surfaces in a complementary pattern – each grid space with an indent on surface A would pair with an empty, or non-indented grid space, on surface B. This configuration doubles the increase in surface area that is gained through the addition of indents to the surface and results in an indentation on one of the surfaces at every grid location. Another advantage of this method is that material property validation can be performed on both joining surfaces and authentication of the barcode can occur on either surface. The third configuration is to match the indentations on one surface to raised marks on the other surface, essentially creating an interlocking interface. This configuration is expected to provide the greatest increase in bonding

strength, especially in the shear direction, due to the interlocking nature of the joining interface. However, there are some drawbacks to this configuration as well. The first is that the manufacturing of the surface with raised marks is markedly more complex than a flat surface that can later have indentations added to modify the surface. This would presumably be done using additive manufacturing, so at least one of the surfaces in the joint would need to be an AM surface, but this would not be the surface that is getting material validation through the hardness testing. This configuration also requires a very high level of manufacturing accuracy in the location, size, shape, and orientation of both the raised marks and the indents in order to ensure a well-fitted interface between the surfaces.

3.3 Mass Serialization

To test the feasibility of using hardness testing indents for part serialization in the form of a 2D barcode, hardness tests were administered in a grid pattern. Using a specified grid spacing, indents were placed at locations in the grid corresponding to the desired serialization code. The barcodes can be represented by a binary string, where a '1' is represented by a grid location with an indent, and a '0' is represented by a grid location without an indent. When the code is read line by line, top to bottom, it can be represented by a 1D binary string that matches the serialization code for the part.

Another function of the codes that were marked is that they were equidigit, meaning that each 1D binary string contained an equal number of 1's and 0's. This equidigit coding strategy was created for a variety of reasons. First, this coding configuration provides optimal readability for a decoder, and a means of quickly checking the authentication results – if the detected code is not equidigit, then there was either an error in the scanning and detection of the barcode, or the part is not marked with a valid barcode. The other advantages of the equidigit coding scheme are

related to the multiple functionalities that the indents are used for, specifically joining and forensic identification. Using an equidigit code guarantees that any code of a given length will be represented by the same number of indents, thus ensuring a constant and predictable increase in surface area, and thus joining enhancement. This same concept applies to the use of the indents for forensic identification, wherein it is expected that each indent provides a predictable number of bits of unique identifying information, and thus the amount of forensic information provided by a barcode of a given length can be determined using the length of the code, since the number of indents for that specific length will not vary between codes.

A variety of codes were marked on acrylic, polycarbonate, and copper surfaces. These codes were then imaged and analyzed to verify accurate identification of the indents and the corresponding 2D barcodes they represented. The purpose of the experiment was verification of the ability to identify the indents and barcodes through imaging. Overall, 10 different codes were marked in 4 x 4 grids on each of the tested materials. Each code contained 8 indents, for a total of 80 indents in each material.

The image analysis was performed using the Python programming language and the Spyder v. 4.1 IDE (integrated development environment). First, the images were thresholded (binarized) to determine the locations of the indents. Functional thresholding was used in coincidence with clustering of the thresholded pixels. Clustering was performed by adding any ‘dark’ pixels within 2 pixels of an existing cluster in any direction into that cluster in an iterative manner, until all ‘dark’ pixels were assigned to a cluster. Once the clusters were formed, the quality of the thresholding value was determined using the coefficient of variance between the cluster sizes. Thresholding values between the lowest and highest values of histogram peaks were tested for clustering in increments of 5, and the thresholding value with the lowest

coefficient of variance was chosen. To identify the locations of the indents, which correspond to the clusters, any clusters of a size less than half of the average cluster size were thrown out to filter out noise, and the centroids of the remaining clusters were calculated and taken to be the indent locations.

Once the indent locations were calculated, the locations of the indents were then analyzed to determine the 2D barcode. The grid size was calculated using the equidigit coding scheme as the square root of twice the number of indents. The indent locations were then used to fit a grid of appropriate size to the indents, and each grid square was determined to be a '1' if an indent was located in the grid square, or a '0' if there was no indent located in the grid square. In this manner, the indent locations were converted into a binary 2D code, which could then be compared to the intended code that was marked to check decoding accuracy.

3.4 Forensics

Each indent created by hardness testing will contain unique identifying features that can be used for forensic authentication. Through the use of high-resolution image analysis, these features can be determined and used for forensic authentication. Forensically identifying features could include variations in indent placement with respect to centered grid locations, indent orientation, indent size, and edge variations. When multiple indentations are marked in a serialization pattern, the uniqueness of each of the indentations in the pattern, cumulatively, creates a high level of forensic identification of the part. The number of forensic bits for a given grid (or barcode) size can be predicted by using an equidigit serialization code, as discussed above. Using this coding scheme, every serialization code of a given length will have an equal number of indentations containing forensic information. The total amount of forensic information is therefore the product of half the code length (the number of 1's) and the number

of unique bits per indentation. Based on the size of the indentations, it is expected that each indent will contain several hundred bits of unique content, which is more than enough to achieve a level of less than 1 in a billion false matches, as is typically required for forensic validation. This method of part identification is inherently copy-resistant (a key aspect of any forensic process) because the unique identifying features of each indentation are byproducts of the variability of the hardness testing process (robotic arm accuracy, variations in indentation shape/size during hardness testing), and thus cannot be replicated.

Chapter 4 – Results

4.1 Hardness Testing Results

Results obtained from the 20 hardness testing trials for each material are given in Table 2. The results presented here for the AM materials are from the fully dense slabs. The hardness value is presented as the mean hardness value from the 20 trials for each material.

Table 2: Hardness Testing Results

	Acrylic	Polycarbonate	PETG	PLA	ABS
Hardness (Shore D)	90.85	84.60	75.10	74.00	72.70
Standard Deviation	0.49	0.35	0.66	1.25	0.82
COV	0.005	0.004	0.009	0.017	0.010

For the AM slabs printed with varying porosities, the mean hardness for each slab was plotted against the percent fill for each material (Fig. 2). The standard deviations of the hardness measurements were plotted as error bars for each data point. The percent fill refers to the density of the middle, porous layer in the slab, and does not reflect the overall density when factoring the outer fully dense layer.

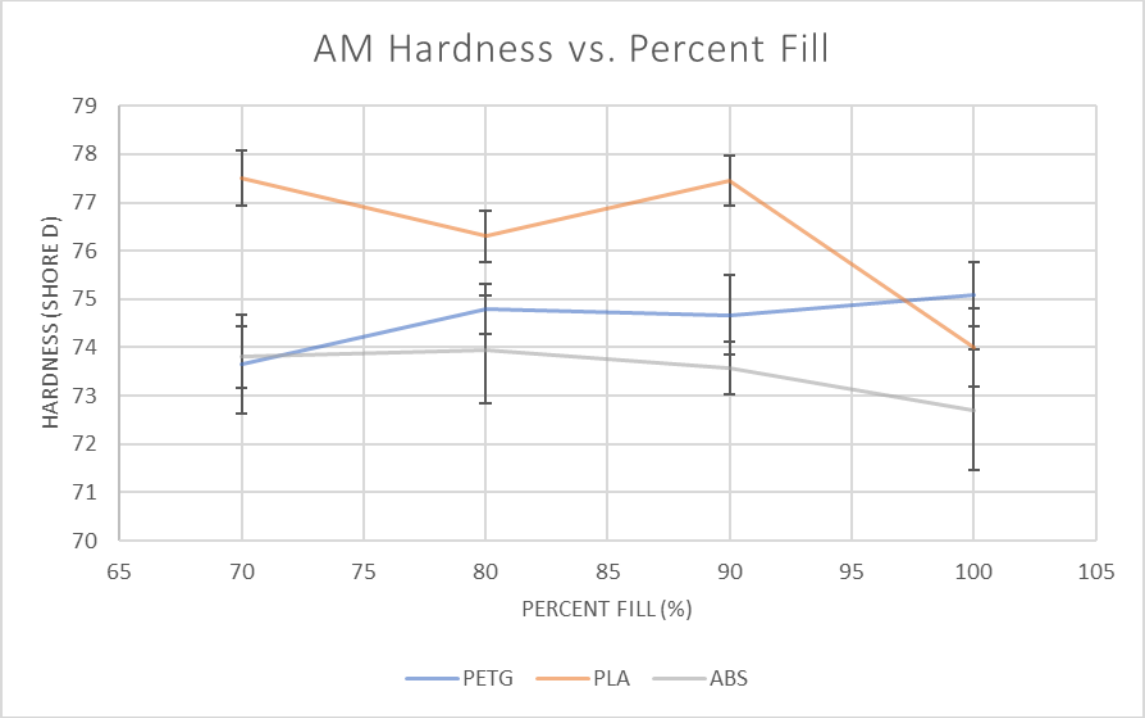

Figure 2: Hardness vs. Percent Fill for AM slabs

The results of the hardness testing performed on the 80% dense cubes with rectilinear and gyroscopic fill patterns are given in Table 3. For the given results, the top face corresponds to the top face of the cube in the build direction. Both the right and front faces were perpendicular to the build direction, as shown in Fig 3.

Table 3: Hardness Testing Results for AM Cubes

		PETG		PLA		ABS	
Fill Pattern		Rect.	Gyro.	Rect.	Gyro.	Rect.	Gyro.
Top Face	Hardness	73.53	73.48	76.83	75.55	73.58	72.73
	Standard Dev	0.44	0.50	0.86	0.89	0.47	1.05
	COV	0.006	0.007	0.011	0.012	0.006	0.014
Right Face	Hardness	70.15	69.68	74.05	72.10	72.65	69.98
	Standard Dev	1.62	0.88	1.75	0.79	1.07	2.31
	COV	0.023	0.016	0.024	0.011	0.015	0.033
Front Face	Hardness	70.90	72.28	71.23	73.95	72.28	71.20
	Standard Dev	1.82	0.80	1.80	0.47	0.95	1.04
	COV	0.026	0.011	0.025	0.010	0.013	0.015

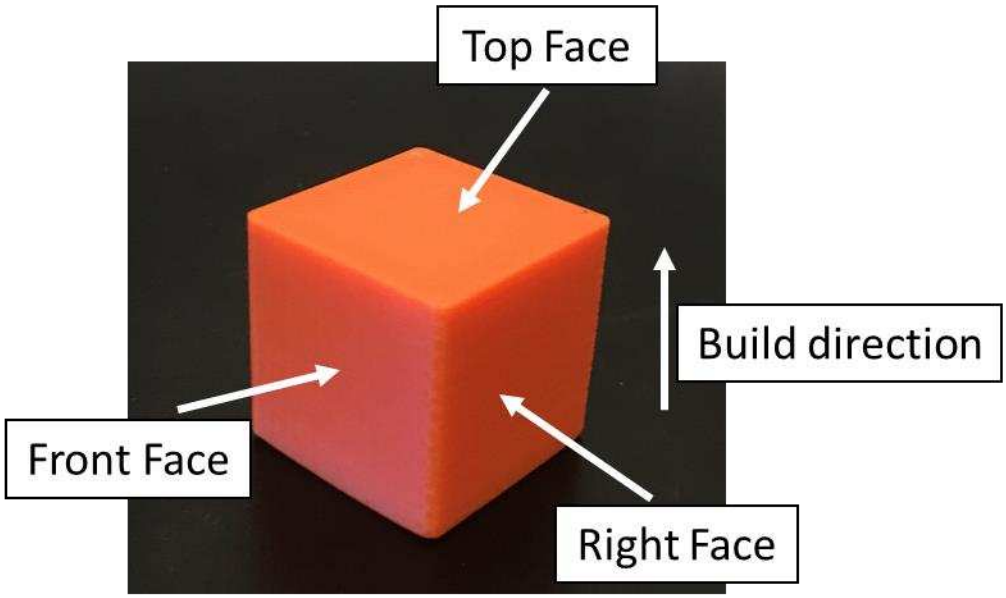

Figure 3: Build Direction and Corresponding Faces for AM Cube Hardness Testing

4.2 Indent Shape Results

The size of the indents created by the hardness testing combinations shown in Table 1 were measured. For square indents, the size was measured as the length of the side of the square, and for circular indents, the size was measured as the radius. The total increase in surface area associated with the average measured indent size and indenter tip shape was then calculated using Equations 1, 2, and 3. These results are calculated for a grid spacing of 1mm, with 50% of grid locations filled with indents. The results are given in Tables 4 and 5.

Table 4: PHT-980 Indent Shape Results

Material	Indent Radius	Percent Increase in Surface Area
Acrylic	0.16 mm	11.5%
Polycarbonate	0.18 mm	14.6%

Table 5: PHT-6005 Indent Shape Results

Material	Indent Width	Percent Increase in Surface Area
Copper	0.31 mm	0.38%

The increase in surface area can also be looked at with respect to the relationship between the indent size and grid spacing. Grid spacing is expected to be a function of indent size since the indent size is one of the main factors controlling the minimum grid spacing. The ratio of indent size to grid spacing also correlates to the information density of the marked grid, as related to forensically identifying information. The indent size will vary between materials and hardness testers, so looking at the increase in surface area as a function of this ratio normalizes the data and provides a better comparison between different indenter tip geometries. The percent increase in surface area is plotted against the ratio of indent size to grid spacing for the two indenter tip geometries that were tested in Figure 4.

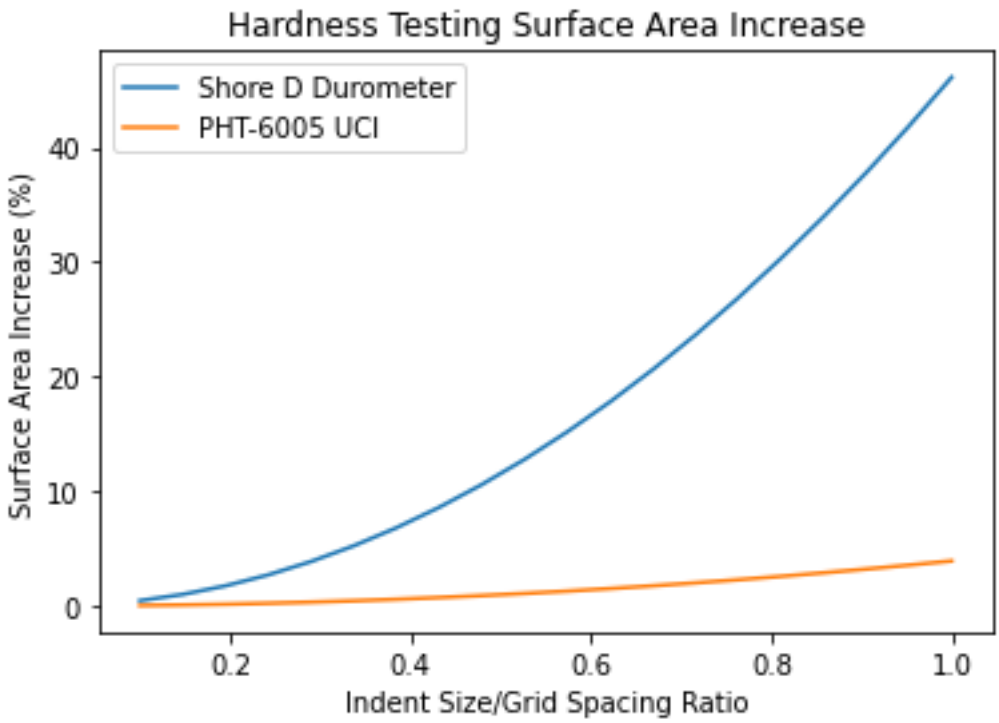

Figure 4: Hardness Testing Surface Area Increase as a Function of Indent Size to Grid Spacing Ratio

4.3 Barcode and Indent Identification Results

There are two adverse results in indent identification that must be considered – the case of false positives (an indent is identified where one does not actually exist), and the case of false negatives (an indent is not identified where one does exist). Because of this, the traditional definition of accuracy is not the best metric for measuring the quality of the indent identification, since it does not account for the false positives which could lead to a misidentification of the marked barcode. A better measure to look at is rate of false positives (false positives per total indents), rate of false negatives (false negatives per total indents), and overall rate of misidentification (sum of rates of false positives and false negatives). Table 6 shows the indent identification results for each of the 3 materials that were used for testing and analysis.

Table 6: Indent Identification Results

Material	False Positive Identifications	False Negative Identifications	Rate of Misidentification
Acrylic	0	0	0
Polycarbonate	0	0	0
Copper	0	0	0

The serialization code identification is dependent on correct indent location identification. Because all of the indents were correctly identified with no false positives, misidentifications did not impact the code authentication results. The results of the code authentication are presented in Table 7, and an example of the image analysis and code identification process is given in Figure 5.

Table 7: Barcode Authentication Results

Material	Barcode Identification Accuracy
Acrylic	100%
Polycarbonate	100%
Copper	100%

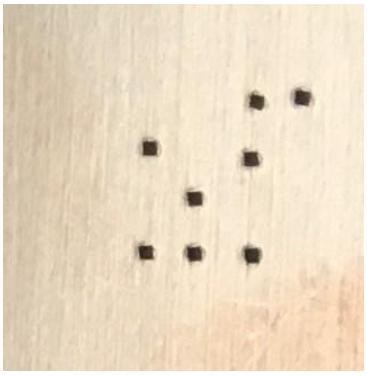

Figure 5a) Original image

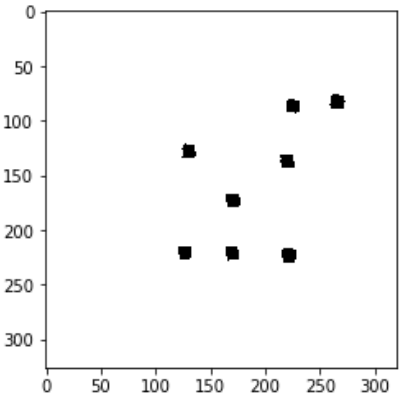

Figure 5b) Thresholded image

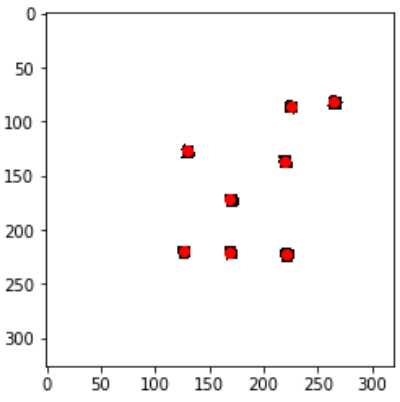

Figure 5c) Calculated mark locations

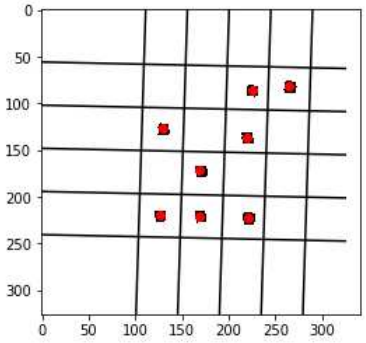

Figure 5d) Calculated grid

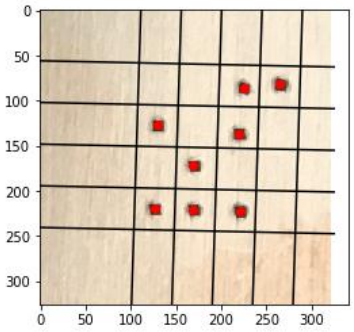

Figure 5e) Final results on original image

0	0	1	1
1	0	1	0
0	1	0	0
1	1	1	0

Figure 5f) Barcode identified from analysis

Figure 5: Barcode Image Analysis and Decoding Process

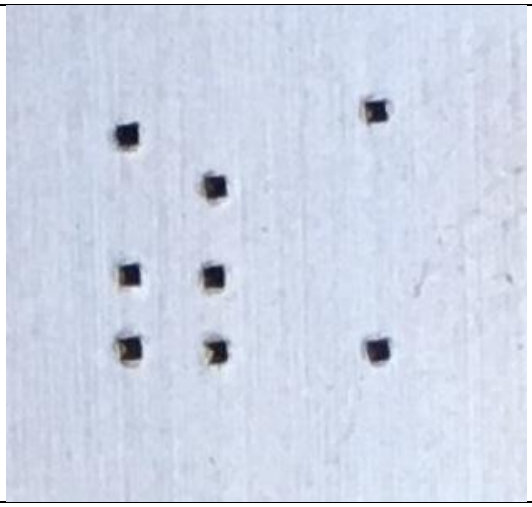

Figure 6a) Indents in copper

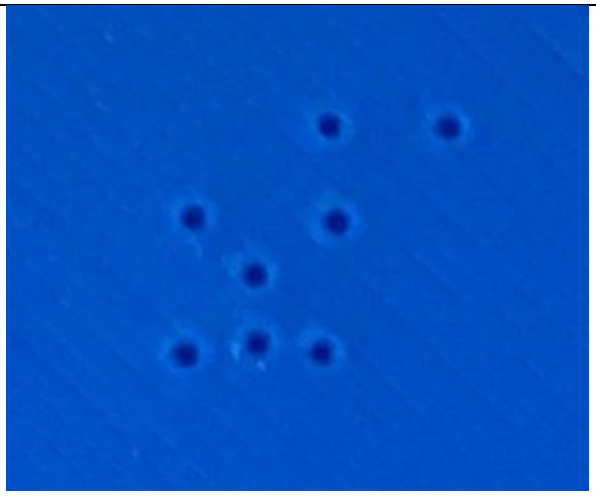

Figure 6b) Indents in PETG

Figure 6: Images of Indents in Various Materials

Chapter 5 – Discussion

5.1 Hardness Testing

The hardness testing results for the AM materials (PETG, PLA, and ABS) had higher standard deviations and coefficients of variance than the traditionally manufactured materials (acrylic and polycarbonate). This is in line with expectations because the AM process introduces more variability within a part, and thus material properties are expected to correspondingly vary more throughout the part compared to traditionally manufactured materials, where the material properties are expected to be consistent throughout the entire material lot. This validates the need for material property testing in AM parts because not only can the material properties vary between parts, but they can also vary within a part, demonstrating the need for validation that material properties are within specifications for the entirety of the part.

However, the hardness testing did not show a correlation between material density and hardness in the AM parts printed with varying densities. One likely cause of this is the fully dense layer on the top of each material slab that was tested. Because the indentations created by the hardness testing are small, they would not fully penetrate this fully dense layer, and thus the porosity beneath this layer is unlikely to be represented by the hardness testing measurement. With such a configuration (a fully dense outer layer), this type of hardness testing is most applicable for mapping surface properties of the part. Additionally, the consistency in the hardness measurements between parts with different porosities validates the ability of hardness testing to validate a material without seeing the effects of porosity, provided there is a sufficiently thick fully dense top layer for testing. However, more testing would be necessary to determine the internal properties of the part. It is possible that different combinations of types of

hardness testing, materials, and print configurations (e.g. fully dense top layer thickness) would allow hardness testing to be used to determine material porosity. More testing would need to be done to determine which combinations of parameters would allow for this if so desired.

For the AM cubes where hardness testing was performed on three orthogonal faces, no statistically significant difference was seen between fill patterns, even though the gyroscopic fill pattern was expected to demonstrate more isotropic properties. One potential cause of this is the effect of the fully dense outer layer, similar to what was seen with the slabs of varying porosities. If the fully dense top layer is thick enough to mask the effect of the porosity on the hardness testing results, then we would not expect to see a difference in hardness measurements between fill patterns. It should be noted that the hardness measured on the top faces of the cubes was consistently higher than the hardness on the other two measured faces (right and front) of the cubes. It is possible this is a result of the fully dense outer layer in the XY build direction (corresponding to the right and front faces) being thinner (0.9 mm) than the fully dense top layer (1.0 mm). Another possibility is that these measurements represented the anisotropic properties of a fully dense build, rather than the gyroscopic isotropic properties from the internal fill pattern.

5.2 Binding/adhesion

The results calculating the increase in surface area which occurs from administering hardness tests showed a large variance based on indenter tip geometry. The main factor affecting the increase in surface area per indent is the tip angle of the indenter – a sharper tip angle results in a greater increase in surface area for a given indent size. This is seen in the fact that the Shore D Durometer, with a tip angle of 30 degrees, creates a much larger increase in surface area at a given indent size to grid spacing ratio than the PHT-6005 UCI hardness tester, with a tip angle of

136 degrees. It should be noted that in increase in surface area produced by the PHT-6005 UCI hardness tester in copper was small enough to be negligible, and so the main effect of those indents would be to increase the surface roughness. The effect of tip angle (indenter tip geometry) on the increase in surface area should then be taken into account when selecting a portable hardness tester for the process described herein, specifically in the case where one of the goals of administering the hardness testing grid is to use the surface for joining with enhanced adhesion. This function is more likely necessary for plastics, which also demonstrated a higher percent increase in surface area from the hardness testing indents due to the type of hardness tester (Shore durometer) that is used for plastics.

However, it should also be noted that the increase in surface area is not the only way that the indents improve joining. Indents of any shape serve to rough up the surface, creating better shear behavior, and thus enhancing the joining properties of the surface. It may also be the case that there is a limit to how acute the angle of the indent can be before the adhesive is unable to penetrate the entire indent; therefore, the full increase in surface area from the indent is not utilized for increasing the area of the binding surface. Other parameters of indent shape may also affect this. Therefore, other factors should also be considered when selecting a portable hardness tester, such as indent size for the material that is being tested, and any minimum size or thickness requirements of the material being tested for the hardness tester.

5.3 Serialization

The results presented in this thesis validate the methodology of using hardness testing indents to mark a serialization code on a part. However, tests were only conducted with 3 different combinations of materials and hardness testers. It is possible that indent identification accuracy will vary with different combinations of materials and indent geometries. Another

factor that must be considered is the optimal imaging parameters that will provide an image sufficient for indent and pattern identification. It is likely some of these parameters, such as lighting, will change with the material that is being imaged.

Further development of the code analysis algorithm would also be necessary for deployment of this methodology. While the code used was sufficient for proof-of-concept, the algorithm needs to be more robust to changes in image quality and orientation, and corrections for misidentification of indents (e.g. error checking that the number of indents matches an equidigit grid size and reidentifying accordingly). Much work has been done in the area of 2D barcode recognition that would be applicable in this space.

Chapter 6 – Conclusion

A process was presented by which hardness testing is used for simultaneous material validation, mass serialization, and forensic authentication, with the added benefit of providing a joining advantage by increasing surface area on the marked surface. The indents created by the hardness testing process can be marked in a specific grid pattern to create a 2D barcode on the part, which can be used for track-and-trace. The plurality of indents also increases the accuracy of the hardness testing for material validation, and gives the opportunity for property mapping over a surface, which is especially advantageous in AM parts where the material properties may vary throughout a part. Analysis of images of 2D barcodes created by hardness testing indents demonstrated accurate indent and pattern identification, validating this as a method of part serialization.

The joining advantage for improved adhesion that is gained by adding indents to a surface was explored by looking at the increase in surface area available for bonding for different indent shapes, spacings, and sizes. The expected increase in surface area depends on two main factors – indent shape, and indent size to grid spacing ratio. For the indent shape, the main factor affecting the increase in surface area is the tip angle of the indenter, with smaller tip angles providing a much greater increase in surface area due to the indents being much deeper for a given size. A higher indent size to grid spacing ratio also results in a greater percent increase in bonding surface area for the marked area. However, this is limited by process and image analysis considerations, which must be accommodated to ensure there is no overlap of indents, and the marked codes can still be correctly identified.

Use of high-resolution image analysis of the indents was also discussed for forensic authentication, wherein unique identifying features of each indent, such as size, shape, and edge variations, combined with unique features of each pattern, such as indent location with respect to theoretical grid center, and indent orientation, can be used to provide a large number of bits of unique information associated with each pattern, and thus a high level of forensic authentication.

Furthermore, an equidigit coding scheme was introduced, in which each barcode contains an equal number of 1's and 0's. This provides a number of advantages for the other functions of the indents in this multi-function process, in addition to improving the readability of the code by providing a simple means of error-checking. Using an equidigit code means that there is a predictable number of indents for a code of any given length. This, in turn, provides a predictable increase in surface area for the function of enhanced joining in adhesive joints, and a predictable amount of forensic information based on the expected amount of unique forensic information provided by a single indent.

A potential application of this process is in the binding of parts manufactured using dissimilar processes, such as bonding of an injection molded part to an AM part. In many cases, AM can be used to design more streamlined and complex parts. However, size constraints and other limitations in the AM process can be limiting to the parts that can be manufactured. This can be solved through joining of AM parts to parts manufactured through other means to maintain the complexity afforded through AM, while avoiding the AM process limitations. All four functionalities (material validation, serialization, forensic identification, and enhanced joining) are relevant to this use case. Additionally, in the case of part failure, this process would be helpful in determining the forensics of the failure. For example, the indentations which are no longer readable may be indicative of stress concentrations during failure. This information would

help identify vulnerabilities in the manufacturing processes. Finally, this process could be used for asserting copyright, similar to a watermark, with the only feasible means of removal cost being prohibitive for would-be fraudulent agents. The indentations are small enough to be nearly invisible to the casual observer, but under high-resolution imaging can be used to verify the origins of a part.

PART II – IMPLEMENTATION WITH A ROBOTIC ARM

Chapter 7 – Introduction

The process of material validation, mass serialization, and forensic authentication presented in Part I is optimized for use in manufacturing because it combines three critical steps in the validation and authentication process into a single operation, thus streamlining this part of the manufacturing process. In this section, a suggested implementation of the process described in Part I is presented through use of a robotic arm to administer the hardness tests. Using a robotic arm to implement this process provides several advantages, such as adaptability of the process to parts of different shapes and sizes, easy reprogramming to change the barcode that is being marked, and the ability to combine multiple inspection tasks (i.e. hardness testing and imaging) into a single process by mounting multiple sensors to the same robotic arm. The adaptability afforded through implementation using a robotic arm is particularly attractive for AM parts, which are often custom or low-batch, and contain complex geometries. Some process considerations concerning the use of a robotic arm for hardness testing and serialization are discussed with recommendations for a successful implementation.

Chapter 8 – Background

8.1 Robotics in Manufacturing

Automation has been prevalent in manufacturing for a long time, allowing higher throughput while reducing the need for human workers to perform redundant or highly physical tasks. With advancements in robotic technologies, automation has become even more integrated into the manufacturing process. A common use of robotics in manufacturing is as part of an assembly line, and the most common industries using industrial robots are automotive, electronics, and electrical goods. Common functions performed by industrial robots include handling (food handling, bin picking), welding, assembly, painting, and processing (grinding, deburring, milling, etc.) [34]. Another increasingly common use of robotics is in additive manufacturing. The use of robotic arms in additive manufacturing has the advantage of increasing the complexity of the build space from a typical layer-by-layer configuration that is used in traditional 3D printers [35]. Using robotics in manufacturing provides several advantages, with one of the main ones being the flexibility of being able to reprogram the robotic system to perform different tasks to different specifications. Robotics can also provide a high level of precision and repeatability when repeatedly performing the same task.

When robotics were first introduced into the manufacturing space, they were isolated from the human manufacturing workers due to the dangers of robots harming humans that entered their working space. More recently, developments have been made in the space of "collaborative robots," or "cobots." Cobots are designed with many external sensors that provide information about their environment intended to reduce the risk of collision with human workers that enter the working space of the robot. They are also designed to work with humans to

perform certain tasks, sensing input from their human coworkers and adjusting accordingly. These modern robots can even learn desired motions through guidance from a human operator through the desired motion [36]. These developments in robotic technology have allowed robots to become much more integrated into manufacturing processes, and have greatly expanded the applications in which robots can be used in manufacturing. However, there are certain trade-offs with using cobots compared to traditional robots, including that cobots often have greater payload restrictions than traditional non-collaborative robots. On the other hand, using collaborative robots allows robots and human workers to work in the same space, thus optimizing floor space, and collaborative processes with robots and humans have been shown to increase throughput in certain manufacturing scenarios [37].

8.2 Robotics for Sensing and Inspection

Another increasingly common application of robotics is for sensing and inspection. Robotics are typically used for these applications in two ways – static inspection of parts during or post-manufacturing, and mobile robotic inspection systems that are used for a wide variety of applications. Static inspection of parts can be achieved by mounting a sensor to the end-effector of a robotic arm. This can be especially useful for inspecting parts during manufacturing processes, such as welding, where in-process inspection can detect problems that occur during manufacturing, but inspection is not feasible without automation that can withstand harsher operating conditions than a human performing the inspection. An example of this is an automated in-process welding inspection system using a robotic arm equipped with an ultrasound for inspection of the weld after each pass [38]. This type of application also streamlines the inspection process because a human operator does not have to repeatedly inspect the weld during the process, thus decreasing the overall process time and increasing throughput. Mobile robotic

inspection systems are typically composed of an unmanned air, ground, or water vehicle that is mounted with a robotic arm or other robotic systems that perform the sensing and inspection tasks. Sensing in these systems includes imaging, laser measurements, temperature measurements, and more. Some applications include infrastructure inspection [39], high-voltage transmission line inspection [40], and inspection in offshore oil and gas producing environments [41]. A major advantage of mobile robotic inspection systems is their ability to operate in harsh or dangerous environments. These robotic systems can also be equipped with additional functionalities to perform maintenance tasks if any adverse findings are detected during the inspection.

8.3 Articulated Robots

Industrial robots are used to accomplish many different kinds of tasks in manufacturing, from assembly to inspection. The most common type of industrial robot is an articulated robot. Articulated robots, also referred to robotic arms, can achieve up to 6 degrees of freedom of motion, making them ideal for a variety of tasks in manufacturing. Additionally, there is a high degree of versatility for different tools to be attached to the end-effector of the robotic arm, allowing the same configuration of robot to be used for many different tasks. The standard configuration for a 6DOF articulated robot arm consists of 6 revolute joints with a 3R (3 revolute joints) ortho-parallel basis structure and a 3R spherical wrist, as shown in Figs 7 and 8 [42].

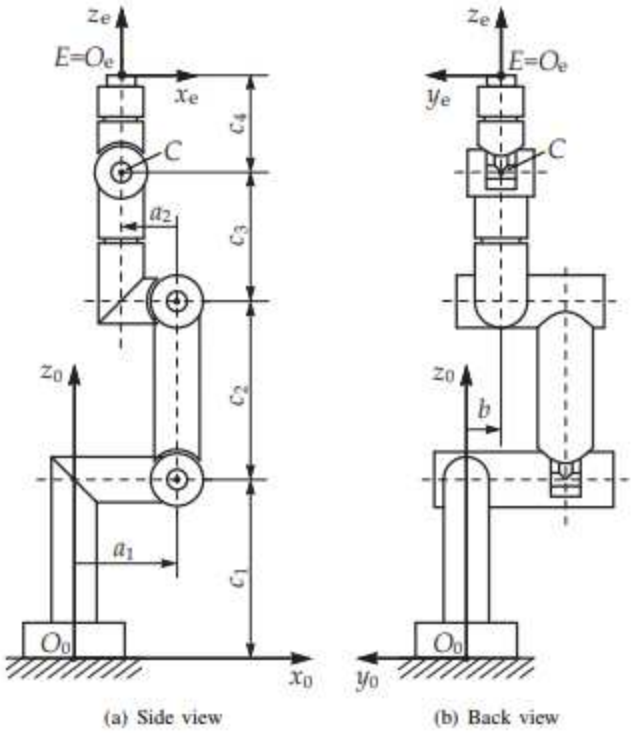

Figure 7: Standard 6DOF robotic arm configuration [42]

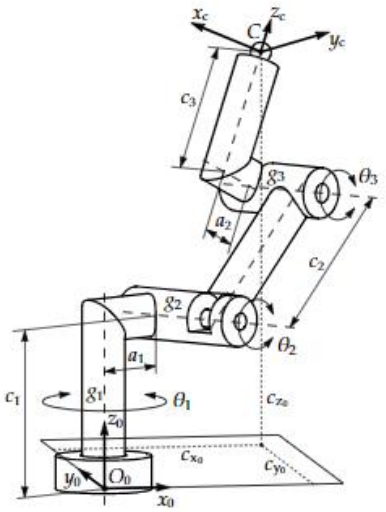

Fig 8a) Ortho-parallel 3R configuration

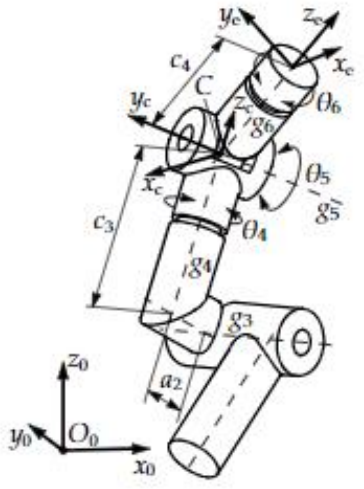

Fig 8b) Spherical wrist 3R configuration

Figure 8: Sub-configurations of 6DOF robotic arm [42]

Chapter 9 – Methods

Robotic arms provide a high degree of flexibility for automation in manufacturing. Two important advantages that are provided by robotic arms are (i) a large range of motion, both spatially and orientationally, and (ii) the ability to be easily reprogrammed to perform either the same task to a different set of specifications, or a different task altogether. Both of these features are critical to the implementation of the hardness testing serialization process using a robotic arm.

The implementation is achieved by mounting a portable hardness tester to the end-effector of a robotic arm. The type of portable hardness tester will depend on a variety of factors, such as the material being tested, indent shape/size preference, etc., and should be chosen with the application-specific case in mind. The robotic arm can then be programmed to administer the hardness tests in a grid pattern to create a 2D barcode, with the ability to modify the following parameters on a part-by-part basis: (i) marking surface location, (ii) marking surface orientation, (iii) grid size, (iv) grid spacing, (v) grid orientation, (vi) indent orientation (if non-circular), and (vii) serialization code. Modifying any of these parameters requires no change of setup to the robotic arm or the part fixturing during the process because all of these parameters are handled in the code controlling the robot. This saves considerable manufacturing time, since changing the setup requires time and introduces more opportunities for mistakes in the setup which could lead to even more lost time, or even potentially scrapped parts.

The flexibility provided by a robotic arm caters especially to additive manufactured parts, which often have complex geometry and are produced in small batch sizes, so the ability to quickly change the testing parameters becomes even more important. The extended range of

motion and ability to reach around obstacles of a robotic arm are also relevant to the implementation of this process for AM parts. Due to the potential for complex geometries of AM parts, the desired testing/marking surface may be in a hard-to-reach location, necessitating a greater degree of flexibility for the test administrator. It is also possible to mark grids on non-flat surfaces (with the appropriate hardness tester selection) with a robotic arm, which could be desirable for AM parts that may not contain flat surfaces for material validation testing.

9.1 Robotic Arm Programming

There are many different frameworks for controlling industrial robotic arms, which vary with the robotic arm manufacturer. Some companies have developed their own control software to be used exclusively with their robotic arms with many built-in functions that allow for only top-level programming for the user. There are also many open-source methods of controlling robotic arms, with the most common being Robot Operating System (ROS). ROS is an open-source software that contains many different libraries and functions compatible with a wide variety of robots and applications. Another option is to control a robot through base code written in a common programming language such as Java, C, or Python. There are also some existing open-source libraries that can be used with these languages for various robotic systems.

The process described in this thesis was prototyped using a WidowX250-6DOF robotic arm. This robotic arm uses the standard 6 degree of freedom (DOF) industrial design of 6 revolute joints. The robot was controlled using Python. The forward kinematics were calculated using transformation matrices from the Denavit-Hartenberg parameters, where the transformation matrix for a link, i, is calculated as:

$$A_i = \begin{bmatrix} c_{\theta_i} & -s_{\theta_i}c_{\alpha_i} & s_{\theta_i}s_{\alpha_i} & a_i c_{\theta_i} \\ s_{\theta_i} & c_{\theta_i}c_{\alpha_i} & -c_{\theta_i}s_{\alpha_i} & a_i s_{\theta_i} \\ 0 & s_{\alpha_i} & c_{\alpha_i} & d_i \\ 0 & 0 & 0 & 1 \end{bmatrix} \quad (4)$$

The final transformation between the ground and end-effector frames can then be calculated as:

$$T_0^7 = A_1 A_2 A_3 A_4 A_5 A_6 A_7 \quad (5)$$

This calculation expresses the position and orientation of the end-effector of the robotic arm in terms of the fixed ground coordinate frame for a given vector of joint positions, θ.

While this calculation determines the robot position for a given joint configuration, it is desirable to control the robot by commanding a desired position and orientation of the end-effector. This requires a solution to the inverse kinematics problem, which solves the required joint positions that will result in a given end-effector position. Because of the configuration of the robot, there are multiple (or no) solutions to this problem for any given position and orientation. Depending on the configuration of the robot, a numerical solution may be required for this problem. However, for the configuration of the robot that was used, an analytical solution can be derived, and this analytical solution (see Appendix A) was used in the control of the robot.

A library of functions was written in the Python programming language to control the movement of the robot in both joint and task space. In joint space, functions were developed for single and multi-joint movements. For the multi-joint movements, the motion could be either asynchronous, in which case each joint moved at its specified velocity regardless of move time, or synchronous, in which case the movement velocity of each joint was adjusted based on the longest joint move time so that all joints would reach the commanded position at the same time.

The movements could also be commanded as relative to current position, or absolute with respect to the 0 (zero) position of each joint. In task space, similar functions were developed for synchronous and asynchronous movements, commanded as either relative moves or absolute moves (both with respect to position in task space). Other functions in the library included functions to set joint velocities and collect data such as motor position, velocity, or current.

Marking grid locations were specified by the orientation of the marking plane, starting mark location, and grid size and spacing. The marking plane orientation was specified using the roll-pitch-yaw convention. Using this convention, both the marking plane and the grid orientation on the marking plane could be fully specified. A function was written that calculates the robot arm position in task space for the given grid specification inputs. These locations were then used to command the robot arm to each grid location. For grid marking, the robot arm was moved into position at a certain offset from the marking surface, then lowered onto the marking surface. These intermediate locations were also calculated with respect to the orientation of the marking surface.

The WidowX250-6DOF robotic arm is actuated by Dynamixel motors. Each of these motors has its own PID controller. The PID gains were tuned for each motor to optimize the tracking performance of the arm, rather than implementing a task space controller. It is common to use this control strategy in industrial robot arms because it eliminates the need for the knowledge of many specific parameters, such as link mass and center of mass location, necessary for a task space controller.

9.2 Process Considerations

There are certain parameters that need to be considered when implementing the process described in this paper with a robotic arm. The first consideration is the accuracy (not the

repeatability, which is more important when the same point in space is accessed many times, as in mass production scenarios) of the robotic arm. This will affect the achievable spatial grid density in the hardness testing process. The grid spacing must be a minimum of double the positional accuracy of the robotic arm. This means that if the robotic arm can move to within a radius of 1mm of given position, then the minimum grid spacing that can be used with that robotic arm is 2mm. This is at the very limit of the robotic arm, and a better constraint would be a minimum grid spacing of 2.5 times the accuracy of the robotic arm in order to prevent overlap of indents and ensure suitable readability of the serialization code marked. However, it should be noted that increased grid spacing will decrease the percent increase in surface area from the indents for enhanced joining, and the forensic information density, as discussed later. Thus, it is desirable to use the minimum grid spacing achievable with the robotic arm.

Another consideration is the ability of the robotic arm to provide sufficient force to generate accurate hardness readings. The portable hardness testers described in this paper are actuated by applying force into the material until the tip is sufficiently depressed in the material. If the force is inadequate to achieve this, the hardness readings will be inaccurate and inappropriate for material validation. The required force is dependent on the hardness tester that is being used, the angle of the material surface with respect to gravity, and the material that is being validated.

The amount of expected forensic information for a given code must also be considered in terms of the information density of the serialization codes, specifically with respect to the number of forensic bits of information contained in a code of a given length. Many parts will have limited surface area appropriate for hardness testing and marking indented serialization codes due to part size, geometry, aesthetic concerns, and other factors, making this a salient

concern. There are two parameters that control the potentially-forensic information density of one of these indented serialization codes: (i) the number of bits of information contained in each indentation, and (ii) the spatial density of the grid in which the indentations are located. The forensic information contained in a single indentation is on the order of dozens of bytes for features the size of the indentations, and this value can be considered to be a constant that is determined by the equipment being used – hardness tester, material, and robotic arm. However, the spatial density of the grid is a parameter that can be optimized. Generally, it is desirable to maximize the information density in order to achieve the highest level of forensic authentication using a given area on a part. A higher information density corresponds to a higher spatial density of indentations in the serialization pattern. Theoretically, placing the indentations as close together as possible without overlap will provide the highest level of information density.

However, there are several practical considerations that must be considered when determining the ideal spatial density of the grid. The first consideration is the size of the indentation. This will vary depending on the hardness tester being used and the material that is being tested. Therefore, the selected grid density should be a function of the indentation size for a specific setup. Another consideration is variation in the orientation of the indentations. For any non-circular indentations, the width of the indentation will vary with orientation, and so the spatial grid density should be chosen to prevent overlap between indentations at any orientation. The resolution of the imaging system used to analyze the images of the indentations could also affect the spacing. It is necessary to determine the minimum spacing needed to be able to distinguish between the individual indentations. Finally, it is likely there will be some variation in the location of the center of each indentation relative to the center of the grid square in which it is located. Practically, this limit will be governed by the accuracy of the robotic arm

administering the indentations, as discussed previously. Additionally, these slight variations in location can be used as forensic identifying information and could be augmented intentionally if the inaccuracies of the robotic arm were too small to provide sufficient forensic information. This is analogous to adding forensic bits of content to surface manufacturing approaches such as 2D and 3D printing with layout variability [43]. The spatial density must be low enough that the indentations will still be identified in the correct grid locations at the extents of the expected deviations from the grid center locations. In order to determine the achievable spatial grid density, all of these factors must be added up to ensure correct pattern identification. Once the achievable spatial grid density and corresponding information density is determined, the number of indentations needed to achieve a given amount of forensic information can be calculated. Using an equidigit code, the length of the code can then be calculated as twice the number of indentations, since half of the digits (the 1's) will contain forensic information.

It is possible to achieve the same amount of forensic information with a shorter code that is repeated (with implementation in cells as described above), rather than a single unique binary string (so long as the shorter string achieves the mass serialization length requirements). Using this method does not sacrifice any forensic information, which is conveyed through the indentations themselves, and is independent of the structure (unique or repeated cells) of the serialization marking.

9.3 Robotic Arm Testing

The grid marking process was prototyped using the WidowX250-6DOF robotic arm. Because of the payload limitations of the arm (250g), it was unable to apply sufficient force to administer hardness tests using the portable hardness testers that were used for the experiments in Part I. Instead, the grids were marked using a pen attached to the end-effector of the robotic

arm to verify both the function library created for the robot arm motion and position calculations, and the ability of the robotic arm to mark a 2D barcode pattern that could be authenticated correctly.

Figure 9: Robotic arm grid marking test setup

Chapter 10 – Results

Testing of the robotic arm validated the equations used for the forward and inverse kinematics, as well as the calculations performed to calculate the grid marking locations for grids on various planes. A sample grid marked by the robotic arm is shown in Fig 10. The smallest achievable grid spacing with this robotic arm was determined to be 3mm. This was at the limit of the accuracy of the robotic arm, and smaller grid spacings resulted in overlap between marks.

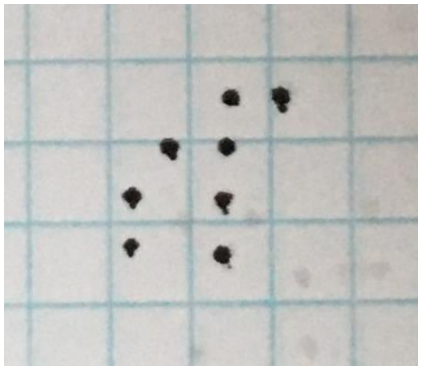

Figure 10: Example barcode marked by robotic arm (4mm spacing)

Chapter 11 – Discussion

The prototyping of this process was limited by the capabilities of the robotic arm that was used. However, the experiments that were performed were still able to show proof of concept for using a robotic arm to mark 2D serialization codes. The equations used for the robot kinematics and grid location calculations were also validated through the experiments. In an actual application setting, a much more robust robotic arm would need to be used to ensure the ability to generate adequate force to perform the hardness testing, as well as sufficient accuracy to achieve the desired grid spacing.

The framework of implementation of an inspection and validation process using a robotic arm presented in this section can be extended beyond the hardness testing procedure described in Part I. There is a wide variety of sensors and associated inspection processes that could be implemented by attaching a sensor to the end-effector of a robotic arm. A potential example of this would be the use of ultrasound for material inspection and flaw detection. In this case the scanning ability of the robotic arm would complement well with the ultrasound material inspection procedure, where the entire surface of the material must be scanned for a full inspection of the part. Other potential sensing applications include electrical conductivity and thermal conductivity, among others. Any number of sensors could be accommodated on the end-effector of the robotic arm to provide multiple sensing functions simultaneously, so long as they meet the payload limit constraint of the robotic arm being used.

Chapter 12 – Conclusion

A methodology for implementing the hardness testing procedure described in Part I using a robotic arm was presented. Various considerations for this implementation, such as robotic arm specifications, hardness tester selection, and serialization grid parameters were discussed, with recommendations for choosing these parameters. Validation of the use of a robotic arm for serialization was demonstrated by using the robotic arm to mark grids with a pen attached to the end-effector using a Python software library created to control the robotic arm. Full prototyping of the process using a portable hardness tester should be done with a more robust robotic arm to validate the entire process. The methodology of robotic-arm-mounted sensor inspection and validation presented here has potential applications to various other forms of sensing, beyond just the hardness testing-based process presented here.

References

[1] Hardness, M. (2018). Introduction to Hardness Testing[1]. *Mechanical Testing and Evaluation*, 197–202.

[2] Qi, H. J., Joyce, K., & Boyce, M. C. (2003). Durometer hardness and the stress-strain behavior of elastomeric materials. *Rubber Chemistry and Technology*, *76*(2), 419–435.

[3] Kleesattel, C., & Gladwell, G. M. L. (1968). *The contact - impedance*. *July*, 175–180.

[4] Junek, M., Janovec, J., & Ducháček, P. (2017). Dependence of ultrasonic contact impedance hardness on Young's modulus of elasticity of creep-resistant steels. *Acta IMEKO*, *6*(1), 27–32.

[5] Pavlina, E. J., & van Tyne, C. J. (2008). Correlation of Yield strength and Tensile strength with hardness for steels. *Journal of Materials Engineering and Performance*, *17*(6), 888–893.

[6] Tiryakioğlu, M., Robinson, J. S., Salazar-Guapuriche, M. A., Zhao, Y. Y., & Eason, P. D. (2015). Hardness-strength relationships in the aluminum alloy 7010. *Materials Science and Engineering A*, *631*, 196–200.

[7] Zhang, H. W., Subhash, G., Jing, X. N., Kecskes, L. J., & Dowding, R. J. (2006). Evaluation of hardness-yield strength relationships for bulk metallic glasses. *Philosophical Magazine Letters*, *86*(5), 333–345.

[8] Li, Z., Wang, Q., Luo, A. A., Fu, P., & Peng, L. (2015). Fatigue strength dependence on the ultimate tensile strength and hardness in magnesium alloys. *International Journal of Fatigue*, *80*, 468–476.

[9] Casagrande, A., Cammarota, G. P., & Micele, L. (2011). Relationship between fatigue limit and Vickers hardness in steels. *Materials Science and Engineering A*, *528*(9), 3468–3473.

[10] Hintsala, E. D., Hangen, U., & Stauffer, D. D. (2018). High-Throughput Nanoindentation for Statistical and Spatial Property Determination. *Jom*, *70*(4), 494–503.

[11] Onuike, B., & Bandyopadhyay, A. (2019). Additive manufacturing in repair: Influence of processing parameters on properties of Inconel 718. *Materials Letters*, *252*, 256–259.

[12] Neikter, M., Åkerfeldt, P., Pederson, R., Antti, M. L., & Sandell, V. (2018). Microstructural characterization and comparison of Ti-6Al-4V manufactured with different additive manufacturing processes. *Materials Characterization*, *143*(September 2017), 68–75.

[13] Wei, C., Sun, Z., Chen, Q., Liu, Z., & Li, L. (2019). Additive Manufacturing of Horizontal and 3D Functionally Graded 316L/Cu10Sn Components via Multiple Material Selective Laser Melting. *Journal of Manufacturing Science and Engineering, Transactions of the ASME*, *141*(8), 1–8.

[14] Meng, W., Xiaohui, Y., Zhang, W., Junfei, F., Lijie, G., Qunshuang, M., & Bing, C. (2020). Additive manufacturing of a functionally graded material from Inconel625 to Ti6Al4V by laser synchronous preheating. *Journal of Materials Processing Technology*, *275*(January 2019).

[15] Keist, J. S., & Palmer, T. A. (2017). Development of strength-hardness relationships in additively manufactured titanium alloys. *Materials Science and Engineering A*, *693*(March), 214–224.

[16] Javidani, M., Arreguin-Zavala, J., Danovitch, J., Tian, Y., & Brochu, M. (2017). Additive Manufacturing of AlSi10Mg Alloy Using Direct Energy Deposition: Microstructure and Hardness Characterization. *Journal of Thermal Spray Technology*, *26*(4), 587–597.

[17] Solberg, K., Wan, D., & Berto, F. (2020). Fatigue assessment of as-built and heat-treated Inconel 718 specimens produced by additive manufacturing including notch effects. *Fatigue and Fracture of Engineering Materials and Structures*, *43*(10), 2326–2336.

[18] Davis, M.J. and McGregor, A., (2010). Assessing adhesive bond failures: mixed-mode bond failures explained. *ISASI Australian Safety Seminar, Canberra,* 4-6.

[19] da Silva, L. F. M., Carbas, R. J. C., Critchlow, G. W., Figueiredo, M. A. V., & Brown, K. (2009). Effect of material, geometry, surface treatment and environment on the shear strength of single lap joints. *International Journal of Adhesion and Adhesives*, *29*(6), 621–632.

[20] Dayss, E., Leps, G., & Meinhardt, J. (1999). Surface modification for improved adhesion of a polymer-metal compound. *Surface and Coatings Technology*, *116–119*, 986–990.

[21] Ghumatkar, A., Budhe, S., Sekhar, R., Banea, M. D., & de Barros, S. (2016). Influence of adherend surface roughness on the adhesive bond strength. *Latin American Journal of Solids and Structures*, *13*(13), 2356–2370.

[22] Baburaj, E. G., Starikov, D., Evans, J., Shafeev, G. A., & Bensaoula, A. (2007). Enhancement of adhesive joint strength by laser surface modification. *International Journal of Adhesion and Adhesives*, *27*(4), 268–276.

[23] Garcia, R., & Prabhakar, P. (2017). Bond interface design for single lap joints using polymeric additive manufacturing. *Composite Structures*, *176*, 547–555.

[24] Dugbenoo, E., Arif, M. F., Wardle, B. L., & Kumar, S. (2018). Enhanced Bonding via Additive Manufacturing-Enabled Surface Tailoring of 3D Printed Continuous-Fiber Composites. *Advanced Engineering Materials*, *20*(12), 1–9.

[25] Ubaid, J., Wardle, B. L., & Kumar, S. (2018). Strength and Performance Enhancement of Multilayers by Spatial Tailoring of Adherend Compliance and Morphology via Multimaterial Jetting Additive Manufacturing. *Scientific Reports*, *8*(1), 1–10.

[26] Frascio, M., de Sousa Marques, E. A., Carbas, R. J. C., da Silva, L. F. M., Monti, M., & Avalle, M. (2020). Review of tailoring methods for joints with additively manufactured adherends and adhesives. *Materials*, *13*(18).

[27] Lei, P., Claret-Tournier, F., Chatwin, C., & Young, R. (2005). A secure mobile track and trace system for anti-counterfeiting. *Proceedings - 2005 IEEE International Conference on e-Technology, e-Commerce and e-Service, EEE-05*, 686–689.

[28] Weinstein, R. (2005). RFID: A technical overview and its application to the enterprise. *IT Professional*, *7*(3), 27–33.

[29] Wang, M., Wang, C., Ma, R., Hu, W., & Su, M. (2020). Metamorphic barcodes based on lithographically defined microdots incorporating nanoparticles of phase change materials. *Journal of Materials Science*, *55*(14), 5823–5831.

[30] Trenfield, S. J., Xian Tan, H., Awad, A., Buanz, A., Gaisford, S., Basit, A. W., & Goyanes, A. (2019). Track-and-trace: Novel anti-counterfeit measures for 3D printed personalized drug products using smart material inks. *International Journal of Pharmaceutics*, *567*.

[31] Simske, S. J., & Adams, G. (2010). High-resolution glyph-inspection based security system. *2010 IEEE International Conference on Acoustics, Speech and Signal Processing,* 1794-1797.

[32] Pollard, S. B., Simske, S. J., & Adams, G. B. (2010). Model based print signature profile extraction for forensic analysis of individual text glyphs. *2010 IEEE International Workshop on Information Forensics and Security, WIFS 2010*.

[33] Ueno, R. (n.d.). *Barcode Fingerprinting: Individual Identification of Commercial Products Using Print Irregularity in Barcodes*.

[34] Hägele, M., Nilsson, K., Pires, J. N., & Bischoff, R. (n.d.). *54. Industrial Robotics*.

[35] Urhal, P., Weightman, A., Diver, C., & Bartolo, P. (2019). Robot assisted additive manufacturing: A review. *Robotics and Computer-Integrated Manufacturing*, *59*(July 2018), 335–345.

[36] Sherwani, F., Asad, M. M., & Ibrahim, B. S. K. K. (2020). Collaborative Robots and Industrial Revolution 4.0 (IR 4.0); Collaborative Robots and Industrial Revolution 4.0 (IR 4.0). In *2020 International Conference on Emerging Trends in Smart Technologies (ICETST)*.

[37] Matheson, E., Minto, R., Zampieri, E. G. G., Faccio, M., & Rosati, G. (2019). Human-robot collaboration in manufacturing applications: A review. *Robotics*, *8*(4), 1–25.

[38] Javadi, Y., Mohseni, E., MacLeod, C. N., Lines, D., Vasilev, M., Mineo, C., Foster, E., Pierce, S. G., & Gachagan, A. (2020). Continuous monitoring of an intentionally-manufactured crack using an automated welding and in-process inspection system. *Materials and Design*, *191*, 108655.

[39] Lattanzi, D., & Miller, G. (2017). Review of Robotic Infrastructure Inspection Systems. *Journal of Infrastructure Systems*, *23*(3), 04017004.

[40] Debenest, P., Guarnieri, M., Takita, K., Fukushima, E. F., Hirose, S., Tamura, K., Kimura, A., Kubokawa, H., Iwama, N., & Shiga, F. (2008). Sensor-arm - Robotic manipulator for

preventive maintenance and inspection of high-voltage transmission lines. *2008 IEEE/RSJ International Conference on Intelligent Robots and Systems, IROS*, 1737–1744.

[41] Bengel, M., Pfeiffer, K., Graf, B., Bubeck, A., & Verl, A. (2009). Mobile robots for offshore inspection and manipulation. *2009 IEEE/RSJ International Conference on Intelligent Robots and Systems, IROS 2009*, 3317–3322.

[42] Brandstötter, M., Angerer, A., & Hofbaur, M. (2014). An Analytical Solution of the Inverse Kinematics Problem of Industrial Serial Manipulators with an Ortho-parallel Basis and a Spherical Wrist. *Proceedings of Austrian Robotics Workshop 2014.*

[43] S.J. Simske and M. Sturgill, "Extended packaging through addition of readable information to the printing," *2009 International Conference on Digital Printing Technologies*, pp. 201-203, 2009

Appendix A – Robotic Arm Inverse Kinematics Solution

The kinematic structure of the robotic arm used in this thesis (3R ortho-parallel + 3R spherical wrist) can be kinematically decoupled into two separate problems to solve the inverse kinematics analytically. Using this decoupling, the transformation from the base coordinate frame to the end-effector coordinate frame can be expressed as:

$$R = R_3^0 R_6^3 \tag{6}$$

In this expression, R_3^0 represents the positional transformation from the 3R ortho-parallel base of the robot, and R_6^3 represents the orientational transformation from the 3R spherical wrist.

The kinematic decoupling allows the inverse kinematics to be solved as two separate problems by first solving for the first 3 joint variables using the desired wrist center coordinate, calculated by:

$$\begin{bmatrix} c_{x_0} \\ c_{y_0} \\ c_{z_0} \end{bmatrix} = \begin{bmatrix} u_{x_0} \\ u_{y_0} \\ u_{z_0} \end{bmatrix} - d_6 R \begin{bmatrix} 0 \\ 0 \\ 1 \end{bmatrix} \tag{7}$$

Where *c* is the desired wrist center coordinate, and *u* is the desired end-effector position. The wrist transformation matrix can then be determined by:

$$R_6^3 = (R_3^0)^T R \tag{8}$$

The wrist transformation matrix can then be used to calculate the final 3 joint variables.

The analytic inverse solution for any given task space position and orientation is not unique, and up to 8 solutions can be obtained for each position. The full derivation of all joint

position solutions for a given position is presented in [42]. The set of solutions derived in [42] is given below.

$$\theta_{1;i} = atan2\left(c_{y_0}, c_{x_0}\right) - atan2\left(b, n_{x_1} + a_1\right) \tag{9}$$

$$\theta_{1;ii} = atan2\left(c_{y_0}, c_{x_0}\right) + atan2\left(b, n_{x_1} + a_1\right) - \pi \tag{10}$$

$$\theta_{2;i,ii} = \mp \operatorname{acos}\left(\frac{s_1^2 + c_2^2 - k^2}{2 s_1 c_2}\right) + atan2\left(n_{x_1}, c_{z_0} - c_1\right) \tag{11}$$

$$\theta_{2;iii,iv} = \mp \operatorname{acos}\left(\frac{s_1^2 + c_2^2 - k^2}{2 s_2 c_2}\right) - atan2\left(n_{x_1} + 2a_1, c_{z_0} - c_1\right) \tag{12}$$

$$\theta_{3;i,ii} = \pm \operatorname{acos}\left(\frac{s_1^2 - c_2^2 - k^2}{2 c_2 k}\right) - atan2(a_2, c_3) \tag{13}$$

$$\theta_{3;iii,iv} = \pm \operatorname{acos}\left(\frac{s_2^2 - c_2^2 - k^2}{2 c_2 k}\right) - atan2(a_2, c_3) \tag{14}$$

$$\theta_{4;p} = atan2\left(R_{23} c_{1;p} - R_{13} s_{1;p}, R_{13} c_{23;p} c_{1;p} + R_{23} c_{23;p} s_{1;p} - R_{33} s_{23;p}\right) \tag{15}$$

$$\theta_{4;q} = \theta_{4;p} + \pi \tag{16}$$

$$\theta_{5;p} = atan2\left(\sqrt{1 - m_p^2}, m_p\right) \tag{17}$$

$$\theta_{5;q} = -\theta_{5;p} \tag{18}$$

$$\theta_{6;p} = atan2\begin{pmatrix} R_{12} s_{23;p} c_{1;p} + R_{22} s_{23;p} s_{1;p} + R_{32} c_{23;p}, \\ -R_{11} s_{23;p} c_{1;p} - R_{21} s_{23;p} s_{1;p} - R_{31} c_{23;p} \end{pmatrix} \tag{19}$$

$$\theta_{6;q} = \theta_{6;p} - \pi \tag{20}$$

Where,

$$n_{x_1} = \sqrt{c_{x_0}^2 + c_{y_0}^2 - b^2} - a_1 \tag{21}$$

$$s_1^2 = n_{x_1}^2 + \left(c_{z_0} - c_1\right)^2 \tag{22}$$

$$s_2^2 = \left(n_{x_1} + 2a_1\right)^2 + \left(c_{z_0} - c_1\right)^2 \tag{23}$$

$$k^2 = a_2^2 + c_3^2 \tag{24}$$

$$m_p = R_{13}s_{23;p}c_{1;p} + R_{23}s_{23;p}s_{1;p} + R_{33}c_{23;p} \tag{25}$$

$$p = \{i, ii, iii, iv\} \tag{26}$$

$$q = \{v, vi, vii, viii\} \tag{27}$$

All of the possible solutions are shown in Table 8.

Table 8: Inverse Kinematic Joint Solution Configurations

Joint	**1**	**2**	**3**	**4**	**5**	**6**	**7**	**8**
θ_1	$\theta_{1;i}$	$\theta_{1;i}$	$\theta_{1;ii}$	$\theta_{1;ii}$	$\theta_{1;i}$	$\theta_{1;i}$	$\theta_{1;ii}$	$\theta_{1;ii}$
θ_2	$\theta_{2;i}$	$\theta_{2;ii}$	$\theta_{2;iii}$	$\theta_{2;iv}$	$\theta_{2;i}$	$\theta_{2;ii}$	$\theta_{2;iii}$	$\theta_{2;iv}$
θ_3	$\theta_{3;i}$	$\theta_{3;ii}$	$\theta_{3;iii}$	$\theta_{3;iv}$	$\theta_{3;i}$	$\theta_{3;ii}$	$\theta_{3;iii}$	$\theta_{3;iv}$
θ_4	$\theta_{4;i}$	$\theta_{4;ii}$	$\theta_{4;iii}$	$\theta_{4;iv}$	$\theta_{4;v}$	$\theta_{4;vi}$	$\theta_{4;vii}$	$\theta_{4;viii}$
θ_5	$\theta_{5;i}$	$\theta_{5;ii}$	$\theta_{5;iii}$	$\theta_{5;iv}$	$\theta_{5;v}$	$\theta_{5;vi}$	$\theta_{5;vii}$	$\theta_{5;viii}$
θ_6	$\theta_{6;i}$	$\theta_{6;ii}$	$\theta_{6;iii}$	$\theta_{6;iv}$	$\theta_{6;v}$	$\theta_{6;vi}$	$\theta_{6;vii}$	$\theta_{6;viii}$

For control of the WidowX250-6DOF robot, any solutions outside the joint limits of the robot were eliminated. Of the remaining solutions, the solution with the minimum total joint motion from the current position was chosen as the optimal position.